Reuter et al., http://www.jcb.org/cgi/content/full/jcb.201405014/DC1

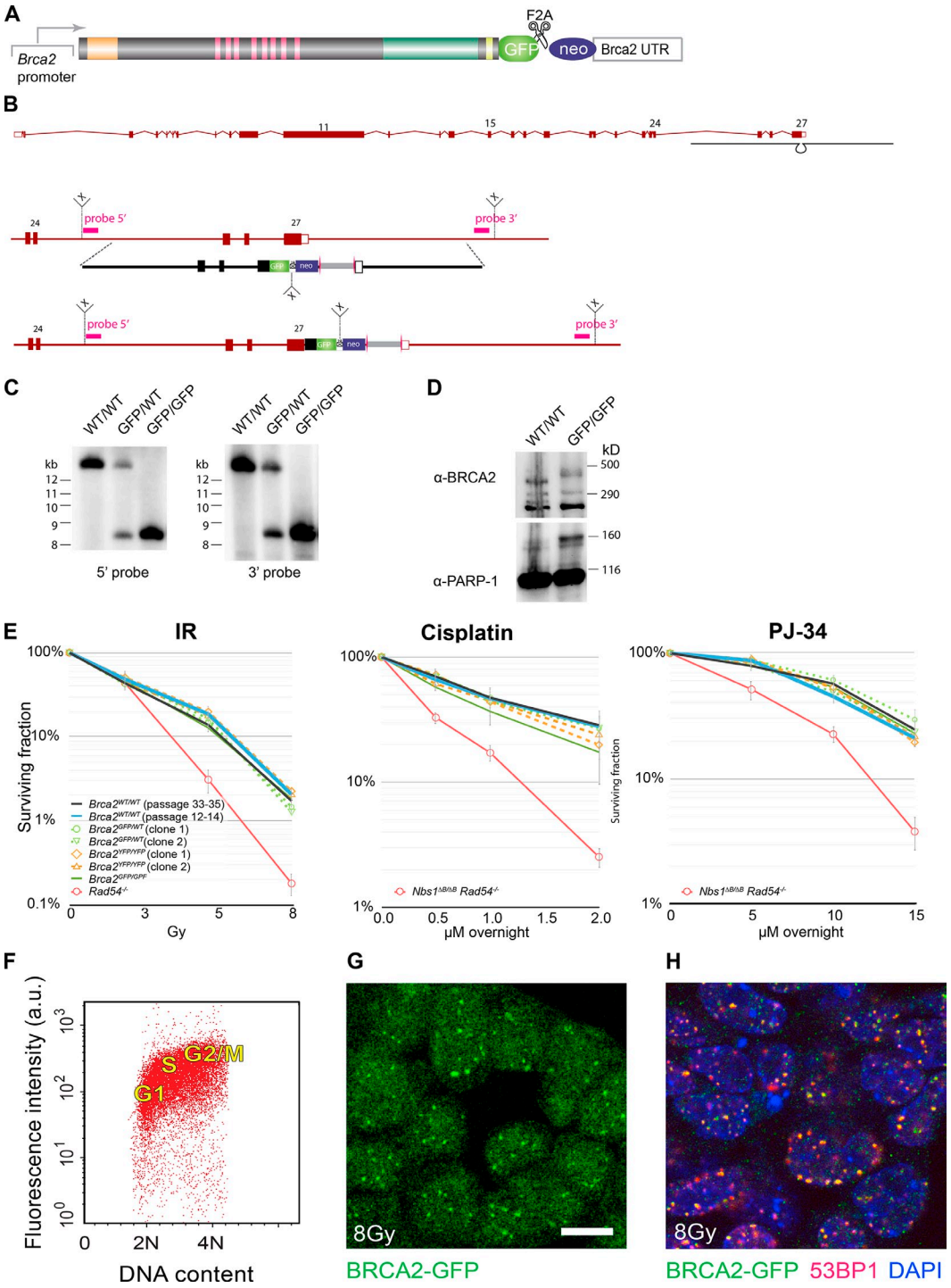

Figure S1. **Generation and characterization of the *Brca2-GFP* knock-in cell lines.** (A) Schematic depiction of the BRCA2-GFP protein expressed from the targeted locus. The self-cleaving F2A peptide sequence ensures separation of the neomycin phosphotransferase protein, used for targeted allele selection, from the BRCA2-GFP fusion. (B) A general schematic of the mouse *Brca2* locus, with the GFP knock-in construct targeting exon 27 indicated in black. Pictured is a *Brca2-GFP* targeting scheme showing wild-type and GFP knock-in alleles and the targeting construct. XbaI restriction sites (X) and probe locations are indicated. (C) Southern blot analysis of the genomic DNA from wild-type, heterozygous, and homozygous *Brca2-GFP* knock-in cell lines digested with XbaI and probed with 5′ or 3′ probe. (D) Western blot analysis of the BRCA2 and BRCA2-GFP expression level in wild-type and homozygous *Brca2-GFP* knock-in cells. (E) Clonogenic survival assays were performed under several IR doses, cisplatin, and PARP inhibitor PJ-34 concentrations with the wild-type (early passage [parental] and later passage, accounting for proliferation during targeted clone derivation) cells and hetero- and homozygous BRCA2-GFP and -YFP knock-in clones. Means of three independent experiments are plotted; error bars represent SEM. (F) FACS plot of $Brca2^{GFP/GPF}$ cells. BRCA2-GFP was fluorescently stained in fixed cells by indirect anti-GFP immunofluorescence and DNA was stained with propidium iodide. (G) BRCA2-GFP accumulates in the characteristic IR-induced foci detected by direct GFP fluorescence with confocal microscopy in cells fixed 2 h after irradiation with 8 Gy. Bar, 10 μm. (H) BRCA2-GFP (direct GFP fluorescence, green) colocalizes with Trp53BP1 (indirect immunofluorescence, red) in IR-induced foci. Cells were fixed 2 h after irradiation with 8 Gy.

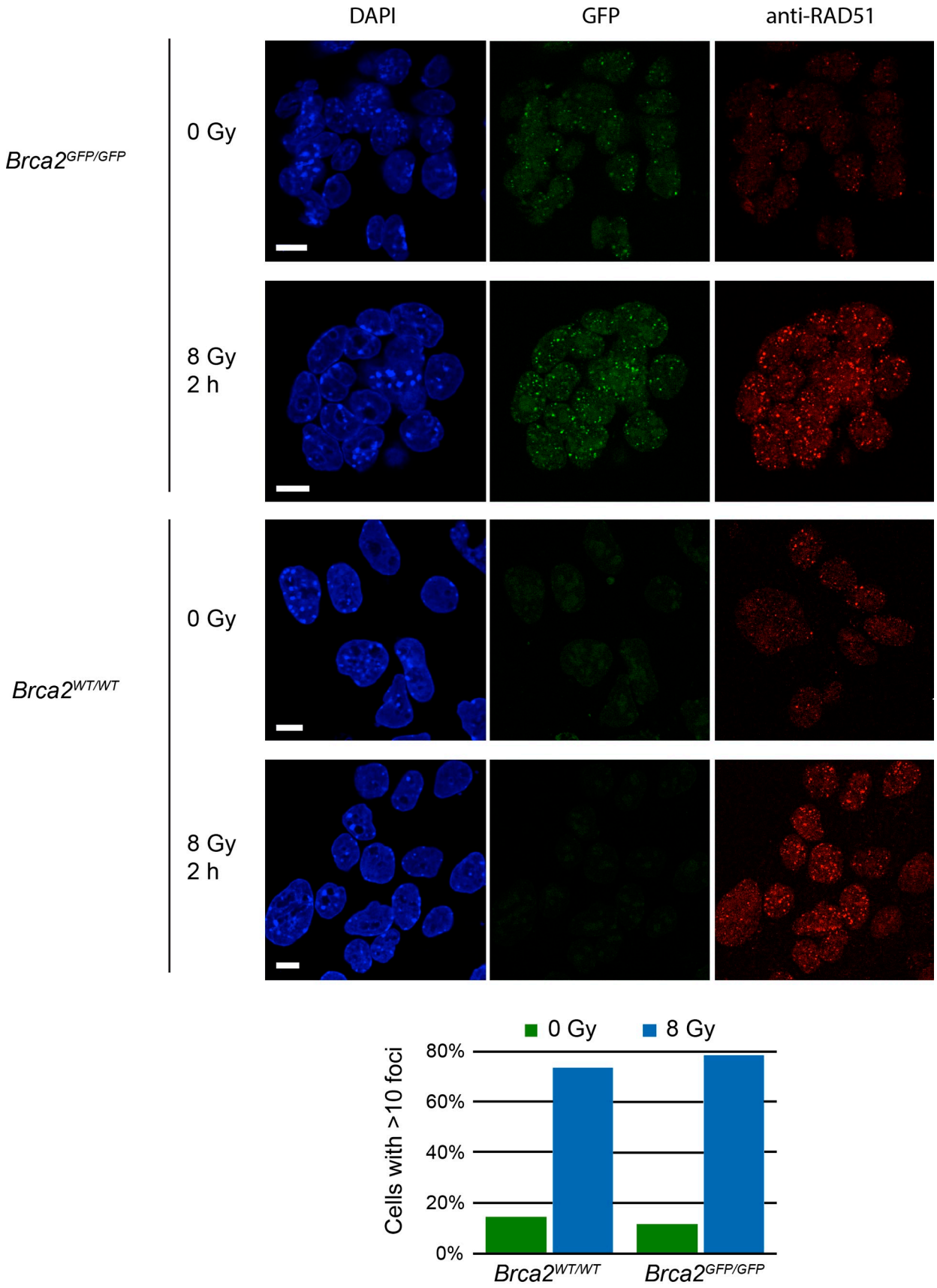

Figure S2. **RAD51 foci induction in *Brca2*$^{GFP/GFP}$ cells.** Confocal microphotographs of wild-type and *Brca2*$^{GFP/GFP}$ cells were stained by indirect immunofluorescence with anti-RAD51 antibody (red). BRCA2-GFP is visualized directly (green); the nuclei of wild-type cells imaged under the same settings emit low levels of background fluorescence. Nuclear DNA is stained with DAPI (blue). The number of RAD51 foci per confocal slice of a nucleus was determined in 30–35 randomly sampled nuclei per each condition. An arbitrary cutoff of 10 foci per nucleus was used to define positive cells. Bars, 10 µm.

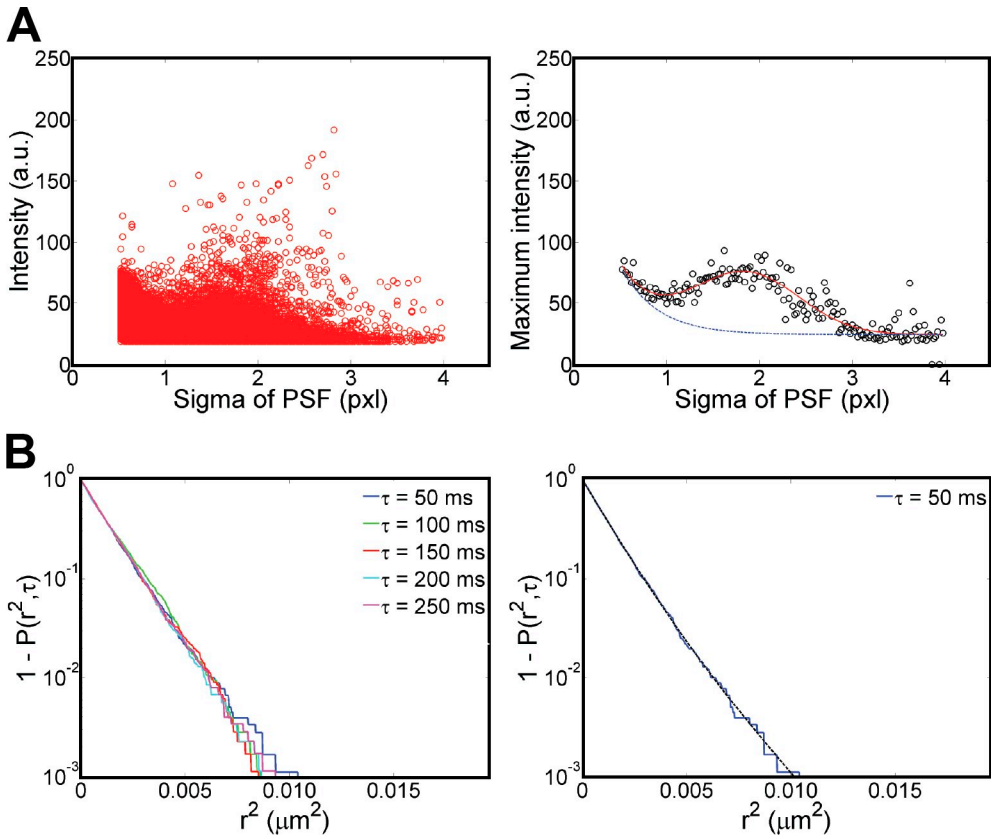

Figure S3. **Defining true single-molecule detections and the limits of diffusion determination by SPT and CDF analysis.** (A, left) The intensity-sigma data pairs were plotted for all detections from one image stack. Camera noise contributes false detections, also found in *Brca2*$^{WT/WT}$ cell nuclei and outside cell nuclei. (A, right) The *n* largest intensity (*n* typically = ~10) values were averaged for each sigma value bin, plotted, and fitted by the sum of a Gaussian and an exponential function (red solid curve). Data from *Brca2*$^{WT/WT}$ cell nuclei and detections from areas outside cell nuclei established that the exponential part covers the false detections (blue broken curve). Hence, removal of all data pairs that lie below the approximated exponential curve leaves the true detections (remaining red points in Fig. 1 B). Typically, at least 50–70% of all initial detections are removed in this way, in some cases also up to 90%. (B) Single-particle tracking and CDF analysis was performed with coverslip-attached 36-nm-sized green fluorescent beads, which appear like single molecules. (B, left) The measured CDF curves acquired at 5% laser power overlap for different time increments, confirming that the microscope system is devoid of drift. (B, right) The raw (blue solid line) and fitted data (black broken line) of the CDF curve acquired at 5% laser power are shown for τ = 50 ms acquisition time. Two-component fitting yielded apparent diffusion constants and amplitudes (Table S2) that set a lower limit for determining diffusion parameters using this technique at the chosen (biologically relevant) acquisition conditions.

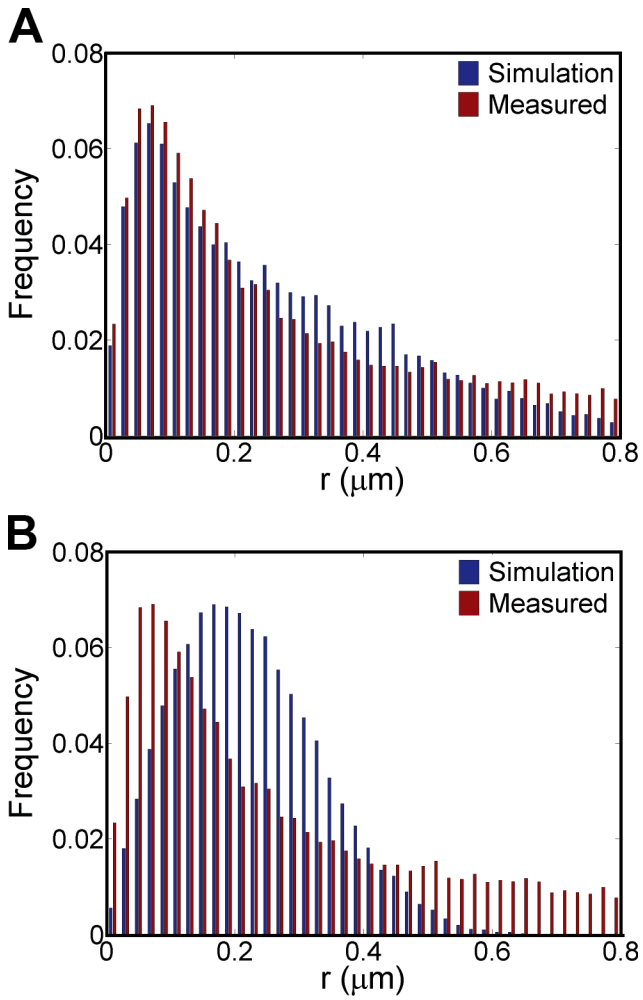

Figure S4. **Single-particle simulations refine the diffusion parameters.** Comparison of the BRCA2-GFP particle jump histogram measured in live, untreated ES cells (red) and matching with simulated SPT data (blue) using $D = 2\ \mu m^2/s$, $\tau_B = 40$ ms, and $\tau_F = 30$ ms (A) and using $D = 0.4\ \mu m^2/s$ without any binding events ($\tau_B = 0$ ms; B). Clearly, the parameter set in A matches the measured data better than the parameter set in B. The goodness of fit was estimated in both datasets using the Kolmogorov-Smirnov (KS) test and the kernel density–based global two-sample comparison test (KD). For $D = 0.4\ \mu m^2/s$, the p-values for the KS and KD test are 2.2×10^{-16} and 5.6×10^{-23}, respectively, showing that the two distributions are significantly different. For $D = 2.0\ \mu m^2/s$, $\tau_B = 40$ ms, and $\tau_F = 30$ ms, the p-values for the KS and KD test are 0.16 and 0.11, respectively, underlining the matching of the two distributions. The test was done with a significance level $\alpha = 0.05$.

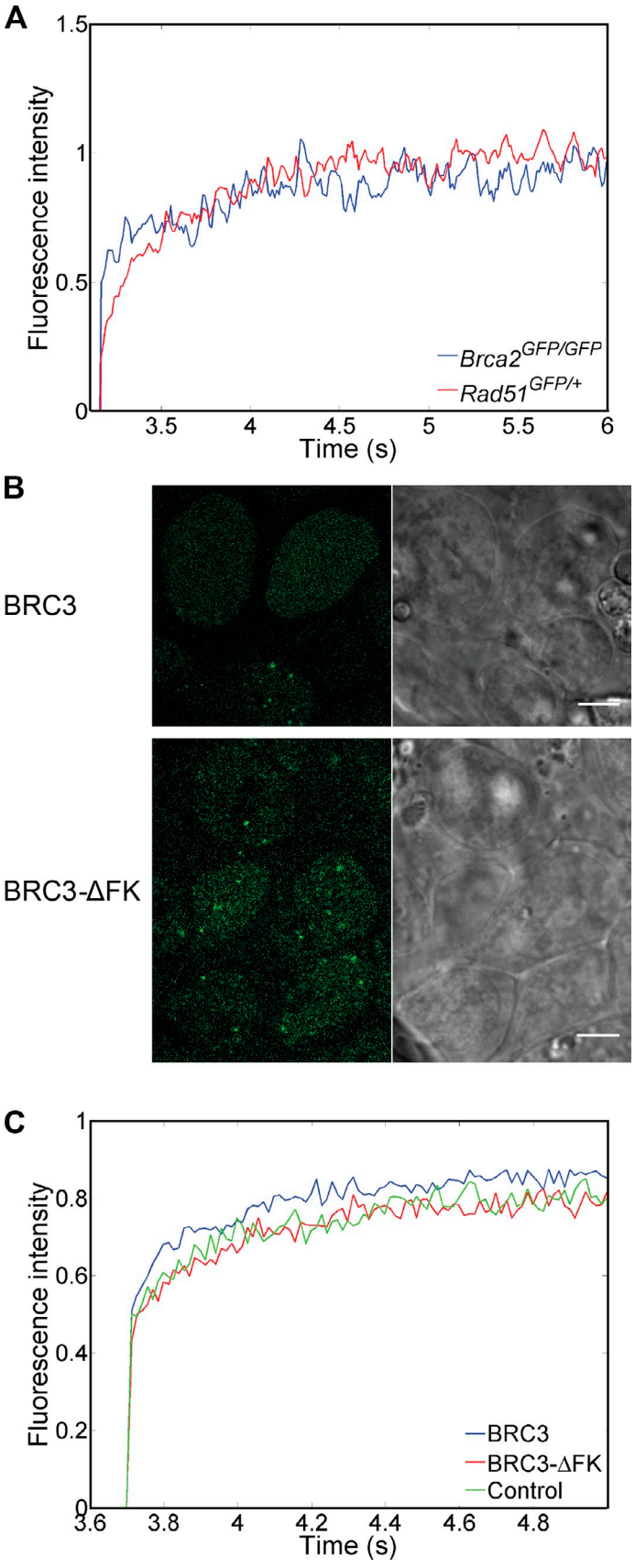

Figure S5. **FRAP measurements of protein mobility in live ES cells.** FRAP assays were performed in live ES cells using *Brca2*$^{GFP/GFP}$ and (transfected) *Rad51*$^{GFP/WT}$ cells. (A) BRCA2-GFP and RAD51-GFP both display slow diffusive (recovery) behavior. In the initial recovery phase of ~350 ms, however, RAD51 displays more stable or longer (transient) binding that is different from BRCA2 but not faster. To compare the diffusive behavior, the postbleach (recovery) part was normalized (as described in the Materials and methods section). The averaged curves were further smoothed by applying a sliding time average window of five subsequent frames. Number of cells (n) = 11 and 13 for the *Brca2*$^{GFP/GFP}$ and *Rad51*$^{GFP/WT}$ cell lines, respectively. (B) Fluorescence and bright-field images of *Rad51*$^{GFP/WT}$ cells expressing a BRC3 or BRC3-ΔFK peptide. Individual cells expressing BRC3 lose their ability to form spontaneous foci and display uniform RAD51-GFP fluorescence indicative of enhanced protein mobility. Cells expressing BRC3-ΔFK fully retain their ability to form and display spontaneous RAD51-GFP foci. Bars, 5 µm. (C) RAD51-GFP recovery changes in *Rad51*$^{GFP/WT}$ cells in response to BRC3 peptide expression due to disruption of BRCA2 binding interactions. To quantify differences in final recovery, data were normalized based on the prebleach area. In the time window of 8–10 s, final recovery values for cells expressing BRC3, BRC3-ΔFK, or no plasmid reached 0.904 ± 0.003, 0.860 ± 0.004, and 0.863 ± 0.005 relative recovery (mean ± 2 × SEM), respectively. This confirms enhanced RAD51 mobility and reduced long-term binding upon BRC3 expression, which is significantly different ($P < 0.05$) from the two control conditions. The number of cells was n = 20, 14, and 8 for the BRC3, BRC3-ΔFK, and control condition, respectively.

Video 1. **BRCA2-GFP diffusion in a live *Brca2*$^{GFP/GFP}$ ES cell.** An individual *Brca2*$^{GFP/GFP}$ nucleus was imaged by oblique illumination using a TIRF setup (Eclipse Ti-E microscope; Nikon). Most BRCA2-GFP particles display only very short-lived transient interactions while diffusing in the nucleus; at time point 5.55 s, two particles are subject to longer-lasting interactions until they diffuse away at time points of 6.2 and 6.6 s. The population of BRCA2-GFP is bleached to a large extent during the 10-s image acquisition period. Spontaneous foci that usually contain tens of proteins and appear stationary were not detected in this field of view. The laser beam passing into the sample had a 75° angle with respect to the objective optical axis. Frames were continuously collected for 10 s using a frame acquisition time of 50 ms. The display rate is 7 frames per second. Compare Fig. 2 (A–C) and Fig. 4 A. Bar, 5 µm.

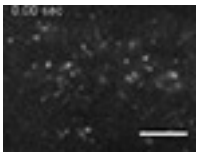

Video 2. **GFP-BRCA2 diffusion in a live HeLa cell.** Nuclei were imaged by oblique illumination using a TIRF setup (Eclipse Ti-E microscope; Nikon). In HeLa cells, GFP-BRCA2 displays the same type of diffusive behavior with transient (binding) interactions and organization into particles containing more than one protein, as was detected for BRCA2-GFP in ES cells. The laser beam passing into the sample had a 75° angle with respect to the objective optical axis. Frames were continuously collected for 10 s using a frame acquisition time of 50 ms. The display rate is 7 frames per second. Bar, 5 µm.

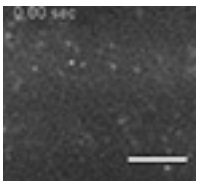

Video 3. **BRCA2-GFP diffusion in a live HeLa cell.** Nuclei were imaged by oblique illumination using a TIRF setup (Eclipse Ti-E microscope; Nikon). In HeLa cells, BRCA2-GFP displays the same type of diffusive behavior with transient (binding) interactions and organization into particles containing more than one protein as was detected for BRCA2-GFP in ES cells. The laser beam passing into the sample had a 75° angle with respect to the objective optical axis. Frames were continuously collected for 10 s using a frame acquisition time of 50 ms. The display rate is 7 frames per second. Bar, 5 µm.

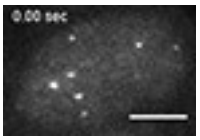

Video 4. **RAD54-GFP diffusion in a live *Rad54*$^{GFP/-}$ ES cell.** An individual *Rad54*$^{GFP/-}$ nucleus was imaged by oblique illumination using a TIRF setup (Eclipse Ti-E microscope; Nikon). Two pools of RAD54 protein in live cells are apparent: fast diffusing RAD54-GFP contributes to uniform nuclear fluorescence, whereas partially bound RAD54 is accumulated in spontaneous foci. By comparison, we can estimate that each of these accumulations contains tens to hundreds of RAD54-GFP molecules. The laser beam passing into the sample had a 75° angle with respect to the objective optical axis. Frames were continuously collected for 10 s using a frame acquisition time of 50 ms. The display rate is 7 frames per second. Compare with Fig. 4 A. Bar, 5 µm.

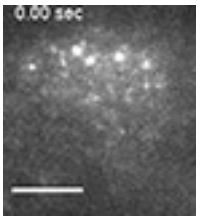

Video 5. **RAD51-GFP diffusion in a live *Rad51*$^{GFP/WT}$ ES cell.** An individual *Rad51*$^{GFP/WT}$ nucleus was imaged by oblique illumination using a TIRF setup (Eclipse Ti-E microscope; Nikon). The nucleus contains both slowly diffusing RAD51-GFP particles and larger (apparently) immobile RAD51 accumulations, often referred to as spontaneous foci. Because of the elevated protein concentration of 50 nM, compared with BRCA2-GFP, not all oligomeric RAD51 entities with few individual proteins can be clearly detected. Note that, in this context, true single molecules will only be detected at concentrations well below 10 nM. The laser beam passing into the sample had a 75° angle with respect to the objective optical axis. Frames were continuously collected for 10 s using a frame acquisition time of 50 ms. The display rate is 7 frames per second. Compare with Fig. 4 A. Bar, 5 µm.

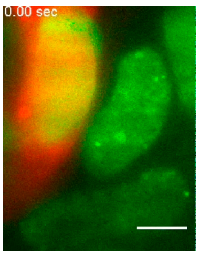

Video 6. **Co-expression of BRC3 and RFP in live *Rad51*$^{GFP/WT}$ ES cells affecting RAD51-GFP diffusion.** Several cells in this field were imaged by oblique illumination using a TIRF setup (Eclipse Ti-E microscope; Nikon). RAD51-GFP and RFP fluorescence is indicated in green and red, respectively. Cells that solely display RAD51-GFP fluorescence are apparently nontransfected and, thus, display spontaneous foci and slowly diffusing RAD51-GFP particles. The red signal observed in one cell indicates sufficient RFP and BRC3 expression so that BRCA2–RAD51 binding is interfered with. This results in uniform RAD51-GFP fluorescence originating from the loss of (transient) binding interactions and concomitant faster diffusion. The laser beam passing into the sample had a 75° angle with respect to the objective optical axis. Frames were continuously collected for 10 s using a frame acquisition time of 50 ms. The display rate is 7 frames per second. Compare Fig. 4 B. Bar, 5 µm.

Table S1. **Mass-spectrometric analysis of GFP pull-down from *Brca2*$^{GFP/GFP}$ and wild-type cells**

Rank	Gene name	Intensity		Sequence coverage		Peptides	
		GFP/GFP	WT/WT	GFP/GFP	WT/WT	GFP/GFP	WT/WT
		log10	*log10*	*%*	*%*		
1	**Brca2**	**10.8**	**NA**	**64.6**	**NA**	**234**	**NA**
2	Hspa8	10.3	10.2	62.7	51.4	47	40
3	Mif	10.2	9.8	67.0	52.2	7	8
4	Eef1a1	10.1	10.3	47.6	44.6	21	18
5	Prdx1	10.1	10.5	73.9	73.9	19	18
6	Eno1	10.1	10.1	54.8	31.9	24	13
7	**Rad51**	**10.0**	**NA**	**58.4**	**NA**	**18**	**NA**
8	Ncl	9.9	10.7	47.9	50.2	48	51
9	Ldha	9.9	10.0	41.0	42.7	20	18
10	Map1b	9.9	9.6	50.1	21.0	110	49.5
17	**Palb2**	**9.7**	**NA**	**42.9**	**NA**	**39**	**NA**
104	**Morf4l1**	**9.2**	**NA**	**52.0**	**NA**	**19**	**NA**
120	**Keap1**	**9.1**	**NA**	**49.0**	**NA**	**26**	**NA**
139	Fanci	9.0	NA	2.3	NA	2	NA
174	**Brca1**	**8.9**	**NA**	**38.1**	**NA**	**60**	**NA**
247	**Morf4l2**	**8.6**	**NA**	**47.6**	**NA**	**14**	**NA**
279	Pcna	8.5	8.8	42.5	42.1	11	10
351	**Bard1**	**8.3**	**NA**	**21.7**	**NA**	**13**	**NA**
455	Xrcc3	8.1	NA	30.7	NA	9	NA
565	Rad51c	7.9	NA	30.3	NA	9	NA
583	Rad50	7.9	7.8	12.8	5.0	16	6
782	Rad51d;Rad51l3	7.5	NA	19.5	NA	5	NA
833	**Bre**	**7.4**	**NA**	**9.9**	**NA**	**3**	**NA**
1,068	Rad51b;Rad51l1	7.0	NA	9.4	NA	3	NA
1,214	**Fam175a**	**6.8**	**NA**	**7.4**	**NA**	**2**	**NA**
1,335	**Bccip**	**6.4**	**NA**	**5.1**	**NA**	**1**	**NA**

The list of proteins identified in the analysis was sorted based on the cumulative intensity, a measure for abundance, in the pull-down from *Brca2*$^{GFP/GFP}$ cells. The 10 top rows are the hits with highest intensity. Other hits are shown only for proteins corresponding to known BRCA complex interactors (indicated in bold) or proteins involved in DNA repair. Some proteins, e.g. DSS1 and EMSY, previously reported as BRCA2 interactors, based on yeast two-hybrid screens, immunoprecipitation of overexpressed tagged proteins, and other assays, were not found in this data, nor are they detected in any similar published mass-spectrometric analysis, despite the high coverage of BRCA2. NA, not applicable.

Table S2. **CDF fit results of immobilized, 36-nm-sized green fluorescent beads (τ = 50 ms)**

Laser power	D_1	A_1	D_2	A_2	σ
%	*$\mu m^2/s$*	*%*	*$\mu m^2/s$*	*%*	*μm*
2.5	0.0097	43	0.0001	57	0.026
5.0	0.0076	18	0.0037	82	0.01
9.5	0.005	13	0.0013	87	0.007

With increasing laser power, the determined apparent diffusion constants become smaller while the weight percentage of the largest found D_{app} value systematically decreases.